

Observation of Events at Very High Q^2 in ep Collisions at HERA

H1 Collaboration

Abstract

Measurements of ep scattering with squared 4-momentum transfer Q^2 up to 35000 GeV^2 are compared with the expectation of the standard deep-inelastic model of lepton-nucleon scattering (DIS). For $Q^2 > 15000 \text{ GeV}^2$, $N_{obs} = 12$ neutral current candidate events are observed where the expectation is $N_{DIS} = 4.71 \pm 0.76$ events. In the same Q^2 range, $N_{obs} = 4$ charged current candidates are observed where the expectation is $N_{DIS} = 1.77 \pm 0.87$ events. The probability $\mathcal{P}(N \geq N_{obs})$ that the DIS model signal N fluctuates to $N \geq N_{obs}$ in a random set of experiments is 6×10^{-3} for neutral current and 0.14 for charged current. The difference in the observed and expected number of Neutral Current events is mostly due to events at large masses $M = \sqrt{x s}$ in which the positron is backscattered at large $y = Q^2/M^2$.

Submitted to Zeitschrift für Physik C

C. Adloff³⁵, S. Aid¹³, M. Anderson²³, V. Andreev²⁶, B. Andrieu²⁹, V. Arkadov³⁶,
 C. Arndt¹¹, I. Ayyaz³⁰, A. Babaev²⁵, J. Bähr³⁶, J. Bán¹⁸, Y. Ban²⁸, P. Baranov²⁶,
 E. Barrelet³⁰, R. Barschke¹¹, W. Bartel¹¹, U. Bassler³⁰, H.P. Beck³⁸, M. Beck¹⁴,
 H.-J. Behrend¹¹, A. Belousov²⁶, Ch. Berger¹, G. Bernardi³⁰, G. Bertrand-Coremans⁴,
 R. Beyer¹¹, P. Biddulph²³, P. Bispham²³, J.C. Bizot²⁸, K. Borrás⁸, F. Botterweck²⁷,
 V. Boudry²⁹, S. Bourov¹¹, A. Braemer¹⁵, W. Braunschweig¹, V. Brisson²⁸,
 W. Brückner¹⁴, P. Bruel²⁹, D. Bruncko¹⁸, C. Brune¹⁶, R. Buchholz¹¹, L. Büngener¹³,
 J. Bürger¹¹, F.W. Büsler¹³, A. Buniatian⁴, S. Burke¹⁹, G. Buschhorn²⁷, D. Calvet²⁴,
 A.J. Campbell¹¹, T. Carli²⁷, M. Charlet¹¹, D. Clarke⁵, B. Clerbaux⁴, S. Cocks²⁰,
 J.G. Contreras⁸, C. Cormack²⁰, J.A. Coughlan⁵, A. Courau²⁸, M.-C. Cousinou²⁴,
 B.D. Cox²³, G. Cozzika⁹, L. Criegee¹¹, D.G. Cussans⁵, J. Cvach³¹, S. Dagoret³⁰,
 J.B. Dainton²⁰, W.D. Dau¹⁷, K. Daum⁴⁰, M. David⁹, C.L. Davis^{19,41}, A. De Roeck¹¹,
 E.A. De Wolf⁴, B. Delcourt²⁸, M. Dirkmann⁸, P. Dixon¹⁹, W. Dlugosz⁷, C. Dollfus³⁸,
 K.T. Donovan²¹, J.D. Dowell³, H.B. Dreis², A. Droutskoi²⁵, O. Dünger¹³, J. Ebert³⁵,
 T.R. Ebert²⁰, G. Eckerlin¹¹, V. Efremenko²⁵, S. Egli³⁸, R. Eichler³⁷, F. Eisele¹⁵,
 E. Eisenhandler²¹, E. Elsen¹¹, M. Erdmann¹⁵, A.B. Fahr¹³, L. Favart²⁸, A. Fedotov²⁵,
 R. Felst¹¹, J. Feltesse⁹, J. Ferencei¹⁸, F. Ferrarotto³³, K. Flamm¹¹, M. Fleischer⁸,
 M. Fliesser²⁷, G. Flügge², A. Fomenko²⁶, J. Formánek³², J.M. Foster²³, G. Franke¹¹,
 E. Fretwurst¹², E. Gabathuler²⁰, K. Gabathuler³⁴, F. Gaede²⁷, J. Garvey³, J. Gayler¹¹,
 M. Gebauer³⁶, H. Genzel¹, R. Gerhards¹¹, A. Glazov³⁶, L. Goerlich⁶, N. Gogitidze²⁶,
 M. Goldberg³⁰, D. Goldner⁸, K. Golec-Biernat⁶, B. Gonzalez-Pineiro³⁰, I. Gorelov²⁵,
 C. Grab³⁷, H. Grässler², T. Greenshaw²⁰, R.K. Griffiths²¹, G. Grindhammer²⁷,
 A. Gruber²⁷, C. Gruber¹⁷, T. Hadig¹, D. Haidt¹¹, L. Hajduk⁶, T. Haller¹⁴, M. Hampel¹,
 W.J. Haynes⁵, B. Heinemann¹¹, G. Heinzelmann¹³, R.C.W. Henderson¹⁹, H. Henschel³⁶,
 I. Herynek³¹, M.F. Hess²⁷, K. Hewitt³, K.H. Hiller³⁶, C.D. Hilton²³, J. Hladký³¹,
 M. Höppner⁸, D. Hoffmann¹¹, T. Holtom²⁰, R. Horisberger³⁴, V.L. Hudgson³, M. Hütte⁸,
 M. Ibbotson²³, C. Issever⁸, H. Itterbeck¹, A. Jacholkowska²⁸, C. Jacobsson²²,
 M. Jacquet²⁸, M. Jaffre²⁸, J. Janoth¹⁶, D.M. Jansen¹⁴, T. Jansen¹¹, L. Jönsson²²,
 D.P. Johnson⁴, H. Jung²², P.I.P. Kalmus²¹, M. Kander¹¹, D. Kant²¹, R. Kaschowitz²,
 U. Kathage¹⁷, J. Katzy¹⁵, H.H. Kaufmann³⁶, O. Kaufmann¹⁵, M. Kausch¹¹,
 S. Kazarian¹¹, I.R. Kenyon³, S. Kermiche²⁴, C. Keuker¹, C. Kiesling²⁷, M. Klein³⁶,
 C. Kleinwort¹¹, G. Knies¹¹, T. Köhler¹, J.H. Köhne²⁷, H. Kolanoski³⁹, S.D. Kolya²³,
 V. Korbelt¹¹, P. Kostka³⁶, S.K. Kotelnikov²⁶, T. Krämerkömper⁸, M.W. Krasny^{6,30},
 H. Krehbiel¹¹, D. Krücker²⁷, A. Küpper³⁵, H. Küster²², M. Kuhlen²⁷, T. Kurča³⁶,
 J. Kurzhöfer⁸, B. Laforge⁹, M.P.J. Landon²¹, W. Lange³⁶, U. Langenegger³⁷,
 A. Lebedev²⁶, F. Lehner¹¹, V. Lemaitre¹¹, S. Levonian²⁹, G. Lindström¹²,
 M. Lindstroem²², F. Linsel¹¹, J. Lipinski¹¹, B. List¹¹, G. Lobo²⁸, G.C. Lopez¹²,
 V. Lubimov²⁵, D. Lüke^{8,11}, L. Lytkin¹⁴, N. Magnussen³⁵, H. Mahlke-Krüger¹¹,
 E. Malinovski²⁶, R. Maraček¹⁸, P. Marage⁴, J. Marks¹⁵, R. Marshall²³, J. Martens³⁵,
 G. Martin¹³, R. Martin²⁰, H.-U. Martyn¹, J. Martyniak⁶, T. Mavroidis²¹, S.J. Maxfield²⁰,
 S.J. McMahon²⁰, A. Mehta⁵, K. Meier¹⁶, P. Merkel¹¹, F. Metlica¹⁴, A. Meyer¹¹,
 A. Meyer¹³, H. Meyer³⁵, J. Meyer¹¹, P.-O. Meyer², A. Migliori²⁹, S. Mikocki⁶,
 D. Milstead²⁰, J. Moeck²⁷, F. Moreau²⁹, J.V. Morris⁵, E. Mroczko⁶, D. Müller³⁸,
 K. Müller¹¹, P. Murín¹⁸, V. Nagovizin²⁵, R. Nahnhauser³⁶, B. Naroska¹³, Th. Naumann³⁶,
 I. Négri²⁴, P.R. Newman³, D. Newton¹⁹, H.K. Nguyen³⁰, T.C. Nicholls³, F. Niebergall¹³,

C. Niebuhr¹¹, Ch. Niedzballa¹, H. Niggli³⁷, G. Nowak⁶, T. Nunnemann¹⁴,
M. Nyberg-Werther²², H. Oberlack²⁷, J.E. Olsson¹¹, D. Ozerov²⁵, P. Palmen²,
E. Panaro¹¹, A. Panitch⁴, C. Pascaud²⁸, S. Passaggio³⁷, G.D. Patel²⁰, H. Pawletta²,
E. Peppel³⁶, E. Perez⁹, J.P. Phillips²⁰, A. Pieuchot²⁴, D. Pitzl³⁷, R. Pöschl⁸, G. Pope⁷,
B. Povh¹⁴, S. Prell¹¹, K. Rabbertz¹, P. Reimer³¹, H. Rick⁸, S. Riess¹³, E. Rizvi²¹,
P. Robmann³⁸, R. Roosen⁴, K. Rosenbauer¹, A. Rostovtsev³⁰, F. Rouse⁷, C. Royon⁹,
K. Rüter²⁷, S. Rusakov²⁶, K. Rybicki⁶, D.P.C. Sankey⁵, P. Schacht²⁷, S. Schiek¹³,
S. Schleif¹⁶, P. Schleper¹⁵, W. von Schlippe²¹, D. Schmidt³⁵, G. Schmidt¹³, L. Schoeffel⁹,
A. Schöning¹¹, V. Schröder¹¹, E. Schuhmann²⁷, B. Schwab¹⁵, F. Sefkow³⁸, A. Semenov²⁵,
V. Shekelyan¹¹, I. Sheviakov²⁶, L.N. Shtarkov²⁶, G. Siegmon¹⁷, U. Siewert¹⁷, Y. Sirois²⁹,
I.O. Skillicorn¹⁰, T. Sloan¹⁹, P. Smirnov²⁶, M. Smith²⁰, V. Solochenko²⁵, Y. Soloviev²⁶,
A. Specka²⁹, J. Spiekermann⁸, S. Spielman²⁹, H. Spitzer¹³, F. Squinabol²⁸, P. Steffen¹¹,
R. Steinberg², J. Steinhart¹³, B. Stella³³, A. Stellberger¹⁶, J. Stier¹¹, J. Stiewe¹⁶,
U. Stöblein³⁶, K. Stolze³⁶, U. Straumann¹⁵, W. Struczinski², J.P. Sutton³,
S. Tapprogge¹⁶, M. Taševsky³², V. Tchernyshov²⁵, S. Tchetchelnitski²⁵, J. Theissen²,
C. Thiebaux²⁹, G. Thompson²¹, P.D. Thompson³, N. Tobien¹¹, R. Todenhausen¹⁴,
P. Truöl³⁸, G. Tsipolitis³⁷, J. Turnau⁶, E. Tzamariudaki¹¹, P. Uelkes², A. Usik²⁶,
S. Valkár³², A. Valkárová³², C. Vallée²⁴, P. Van Esch⁴, P. Van Mechelen⁴,
D. Vandenplas²⁹, Y. Vazdik²⁶, P. Verrecchia⁹, G. Villet⁹, K. Wacker⁸, A. Wagener²,
M. Wagener³⁴, R. Wallny¹⁵, B. Waugh²³, G. Weber¹³, M. Weber¹⁶, D. Wegener⁸,
A. Wegner²⁷, T. Wengler¹⁵, M. Werner¹⁵, L.R. West³, S. Wiesand³⁵, T. Wilksen¹¹,
S. Willard⁷, M. Winde³⁶, G.-G. Winter¹¹, C. Wittek¹³, M. Wobisch², H. Wollatz¹¹,
E. Wunsch¹¹, J. Žáček³², D. Zarbock¹², Z. Zhang²⁸, A. Zhokin²⁵, P. Zini³⁰, F. Zomer²⁸,
J. Zsembery⁹, K. Zuber¹⁶ and M. zurNedden³⁸

¹ *I. Physikalisches Institut der RWTH, Aachen, Germany^f*

² *III. Physikalisches Institut der RWTH, Aachen, Germany^f*

³ *School of Physics and Space Research, University of Birmingham, Birmingham, UK^b*

⁴ *Inter-University Institute for High Energies ULB-VUB, Brussels; Universitaire Instelling Antwerpen, Wilrijk; Belgium^c*

⁵ *Rutherford Appleton Laboratory, Chilton, Didcot, UK^b*

⁶ *Institute for Nuclear Physics, Cracow, Poland^d*

⁷ *Physics Department and IIRPA, University of California, Davis, California, USA^e*

⁸ *Institut für Physik, Universität Dortmund, Dortmund, Germany^f*

⁹ *CEA, DSM/DAPNIA, CE-Saclay, Gif-sur-Yvette, France*

¹⁰ *Department of Physics and Astronomy, University of Glasgow, Glasgow, UK^b*

¹¹ *DESY, Hamburg, Germany^a*

¹² *I. Institut für Experimentalphysik, Universität Hamburg, Hamburg, Germany^f*

¹³ *II. Institut für Experimentalphysik, Universität Hamburg, Hamburg, Germany^f*

¹⁴ *Max-Planck-Institut für Kernphysik, Heidelberg, Germany^a*

¹⁵ *Physikalisches Institut, Universität Heidelberg, Heidelberg, Germany^f*

¹⁶ *Institut für Hochenergiephysik, Universität Heidelberg, Heidelberg, Germany^a*

¹⁷ *Institut für Reine und Angewandte Kernphysik, Universität Kiel, Kiel, Germany^f*

¹⁸ *Institute of Experimental Physics, Slovak Academy of Sciences, Košice, Slovak Republic^{f,j}*

- ¹⁹ *School of Physics and Chemistry, University of Lancaster, Lancaster, UK^b*
²⁰ *Department of Physics, University of Liverpool, Liverpool, UK^b*
²¹ *Queen Mary and Westfield College, London, UK^b*
²² *Physics Department, University of Lund, Lund, Sweden^g*
²³ *Physics Department, University of Manchester, Manchester, UK^b*
²⁴ *CPPM, Université d'Aix-Marseille II, IN2P3-CNRS, Marseille, France*
²⁵ *Institute for Theoretical and Experimental Physics, Moscow, Russia*
²⁶ *Lebedev Physical Institute, Moscow, Russia^f*
²⁷ *Max-Planck-Institut für Physik, München, Germany^f*
²⁸ *LAL, Université de Paris-Sud, IN2P3-CNRS, Orsay, France*
²⁹ *LPNHE, Ecole Polytechnique, IN2P3-CNRS, Palaiseau, France*
³⁰ *LPNHE, Universités Paris VI and VII, IN2P3-CNRS, Paris, France*
³¹ *Institute of Physics, Czech Academy of Sciences, Praha, Czech Republic^{f,h}*
³² *Nuclear Center, Charles University, Praha, Czech Republic^{f,h}*
³³ *INFN Roma 1 and Dipartimento di Fisica, Università Roma 3, Roma, Italy*
³⁴ *Paul Scherrer Institut, Villigen, Switzerland*
³⁵ *Fachbereich Physik, Bergische Universität Gesamthochschule Wuppertal, Wuppertal, Germany^f*
³⁶ *DESY, Institut für Hochenergiephysik, Zeuthen, Germany^f*
³⁷ *Institut für Teilchenphysik, ETH, Zürich, Switzerlandⁱ*
³⁸ *Physik-Institut der Universität Zürich, Zürich, Switzerlandⁱ*
³⁹ *Institut für Physik, Humboldt-Universität, Berlin, Germany^f*
⁴⁰ *Rechenzentrum, Bergische Universität Gesamthochschule Wuppertal, Wuppertal, Germany^f*
⁴¹ *Visitor from Physics Dept. University Louisville, USA*

^a *Supported by the Bundesministerium für Bildung, Wissenschaft, Forschung und Technologie, FRG, under contract numbers 6AC17P, 6AC47P, 6DO57I, 6HH17P, 6HH27I, 6HD17I, 6HD27I, 6KI17P, 6MP17I, and 6WT87P*

^b *Supported by the UK Particle Physics and Astronomy Research Council, and formerly by the UK Science and Engineering Research Council*

^c *Supported by FNRS-NFWO, IISN-IIKW*

^d *Partially supported by the Polish State Committee for Scientific Research, grant no. 115/E-343/SPUB/P03/120/96*

^e *Supported in part by USDOE grant DE F603 91ER40674*

^f *Supported by the Deutsche Forschungsgemeinschaft*

^g *Supported by the Swedish Natural Science Research Council*

^h *Supported by GA ČR grant no. 202/96/0214, GA AV ČR grant no. A1010619 and GA UK grant no. 177*

ⁱ *Supported by the Swiss National Science Foundation*

^j *Supported by VEGA SR grant no. 2/1325/96*

1 Introduction

The ep collider HERA offers the unique possibility to probe the proton at very small distances ($\simeq 10^{-16}$ cm) via t -channel exchange of highly virtual gauge bosons [1, 2, 3], and to search in the s -channel for new particles which couple to lepton-parton pairs with masses up to the kinematic limit of $\sqrt{s} \simeq 300$ GeV [4].

In this paper, measurements of neutral current (NC) and charged current (CC) deep-inelastic scattering (DIS) are considered using all available e^+p data collected by H1 at HERA from 1994 to 1996. The positron beam energy E_e^0 was 27.5 GeV and the proton beam energy E_p was 820 GeV. The total integrated luminosity amounts to 14.19 ± 0.32 pb $^{-1}$, an increase of a factor ~ 5 compared to the above cited earlier studies.

2 The H1 Detector

A detailed description of the H1 detector can be found in [5]. Here we describe only the components relevant for the present analysis in which the final state of the events involves either a positron¹ with high transverse energy or a large amount of hadronic transverse energy flow.

The positron energy and angle are measured in a liquid argon (LAr) sampling calorimeter [6] covering the polar angular² range $4^\circ \leq \theta \leq 153^\circ$ and all azimuthal angles. The granularity is optimized to provide fine and approximately uniform segmentation in laboratory pseudorapidity and azimuthal angle ϕ . It consists of a lead/argon electromagnetic section followed by a stainless steel/argon hadronic section. Electromagnetic shower energies are measured with a resolution of $\sigma(E)/E \simeq 12\%/\sqrt{E/\text{GeV}} \oplus 1\%$ and pion induced hadronic energies with $\sigma(E)/E \simeq 50\%/\sqrt{E/\text{GeV}} \oplus 2\%$ after software energy weighting. These resolutions were measured in test beams with electron energies up to 166 GeV [7, 8] and pion energies up to 205 GeV [8]. The absolute energy scales are known to 3% and 4% for electromagnetic and hadronic energies respectively. The angular resolution on the positron measured from the electromagnetic shower in the calorimeter varies from ~ 2 mrad below 30° to $\lesssim 5$ mrad at larger angles. A lead/scintillating-fibre backward calorimeter [9] extends the coverage³ at larger angles ($155^\circ \leq \theta \lesssim 178^\circ$).

Located inside the calorimeters is the tracking system which is used here to determine the interaction vertex. The main components of this system are central drift and proportional chambers ($25^\circ \leq \theta \leq 155^\circ$), a forward track detector ($7^\circ \leq \theta \leq 25^\circ$) and a backward drift chamber³. The tracking chambers and calorimeters are surrounded by a superconducting solenoid providing a uniform field of 1.15 T parallel to the z axis within the detector volume. The instrumented iron return yoke surrounding this solenoid is used to measure leakage of hadronic showers and to recognize muons. The luminosity is determined from the rate of the Bethe-Heitler $ep \rightarrow ep\gamma$ bremsstrahlung measured in a

¹The analysis does not distinguish explicitly between e^+ and e^- .

²The z axis is taken to be in the direction of the incident proton, and the origin of coordinates is the nominal ep interaction point.

³The detectors in the backward region were upgraded in 1995 by the replacement of the lead/scintillator tile calorimeter [10] and a proportional chamber.

luminosity monitor. This consists of a positron tagger (e -tagger) and a photon tagger (γ -tagger), located -33 m and -103 m respectively from the interaction point.

3 Event Selection and Kinematics

3.1 Selection of ep Collisions

The analysis considers the accumulated data corresponding to H1 running conditions for which the central jet chambers (CJC), the LAr calorimeter and associated triggers, the backward calorimeter, the time-of-flight system and the luminosity system are fully operational. The trigger requirement is either an electromagnetic cluster or a large imbalance in transverse “momentum” $P_{T,miss}^{trig}$ measured with coarse trigger towers of the LAr calorimeter [6]. Every tower k provides a fast energy sum \vec{E}_k which contributes to the reconstruction of $P_{T,miss}^{trig} \equiv \sqrt{(\sum E_{x,k})^2 + (\sum E_{y,k})^2}$.

Background not related to e^+p collisions is first rejected by requiring for each event :

1. a primary interaction vertex in the range $|z - \bar{z}| < 35$ cm where \bar{z} varies within ± 5 cm around $z = 0$ depending on the HERA beam settings;
2. that the event time t_0 determined accurately ($\sigma^{CJC}(t_0) \simeq 1.6$ ns) from the central jet chambers coincides with the nominal time of the bunch crossings of the beams;
3. that it should survive a set of halo and cosmic muon filters [2].

Cut (1) mainly suppresses beam-wall and beam-residual gas interactions. Cuts (2) and (3) eliminate any remaining background produced by cosmic rays and by “halo” muons associated with the proton beam.

3.2 Neutral Current Selection and Kinematics

The following criteria are designed to select NC DIS events in the high Q^2 domain. The cuts, which rely only on calorimetric information, require :

1. an isolated positron with $E_{T,e} > 25$ GeV ($E_{T,e} = E_e \sin \theta_e$), found within the polar angular range $10^\circ \leq \theta_e \leq 145^\circ$; the positron energy cluster should contain more than 98% of the LAr energy found within a pseudorapidity-azimuthal cone of opening $\sqrt{(\Delta\eta_e)^2 + (\Delta\phi_e)^2} = 0.25$ where $\eta_e = -\ln \tan \frac{\theta_e}{2}$;
2. a total transverse momentum balance $P_{T,miss}/\sqrt{E_{T,e}} \leq 3\sqrt{\text{GeV}}$ where $P_{T,miss} \equiv \sqrt{(\sum E_{x,i})^2 + (\sum E_{y,i})^2}$ summed over all energy deposits i in the calorimeters ($E_{x,i} = E_i \sin \theta_i \cos \phi_i$ and $E_{y,i} = E_i \sin \theta_i \sin \phi_i$);
3. a limited momentum loss in the direction of the incident positron, $43 \leq \sum (E - P_z) \leq 63$ GeV, where $\sum (E - P_z) \equiv \sum (E_i - E_{z,i})$ with $E_{z,i} = E_i \cos \theta_i$.

The identification of positron induced showers relies on detailed knowledge of the expected lateral and longitudinal shower properties [7]. The efficiency for the detection of positrons exceeds 90% everywhere within the acceptance cuts, the main losses being due to showers developing through the inactive material between calorimeter modules. The cut (2) makes possible a very efficient NC DIS selection up to the highest Q^2 by taking into account the natural scale of the hadronic energy resolution. The cut (3) retains 90% of NC DIS events and exploits the fact that by energy-momentum conservation, the $\sum (E - P_z)$ distribution for DIS events is peaked at $2E_e^0$. It rejects events where a very hard collinear γ is emitted by the initial state positron.

To calculate the appropriate DIS Lorentz invariants Q^2, y and $M = \sqrt{xs}$, two different sets of estimators are used. Firstly, use is made of only the measurement of the scattered positron:

$$M_e = \sqrt{s x_e} = \sqrt{\frac{Q_e^2}{y_e}}, \quad Q_e^2 = \frac{E_{T,e}^2}{1 - y_e}, \quad y_e = 1 - \frac{E_e - E_e \cos \theta_e}{2E_e^0}.$$

This method will henceforth be denoted the e -method. Secondly use is made of the reconstructed angles θ_e and θ_h of the positron and hadronic final state. Using $\alpha_e = \tan(\theta_e/2) = (E_e - E_{z,e})/E_{T,e}$, and $\alpha_h = \tan(\theta_h/2) = \sum (E_i - E_{z,i})/\sqrt{(\sum E_{x,i})^2 + (\sum E_{y,i})^2}$, where the summations are over all energy deposits of the hadronic final state, then [11] :

$$M_{2\alpha} = \sqrt{\frac{s}{\alpha_e \alpha_h} \frac{E_e^0}{E_p}}, \quad Q_{2\alpha}^2 = \frac{E_e^0}{E_p} \frac{s}{\alpha_e (\alpha_e + \alpha_h)}, \quad y_{2\alpha} = \frac{\alpha_h}{\alpha_e + \alpha_h}.$$

This method will henceforth be denoted the 2α -method. In the parton model, the variable x is interpreted as the momentum fraction carried by a parton in the proton. The centre of mass energy of the positron-parton collision is M . The variable y is related to the polar scattering angle θ_e^* of the positron relative to the incident proton in the centre of mass frame of the positron-parton collision according to $y = (1 + \cos \theta_e^*)/2$.

In addition to the cuts (1) to (3) above, the analysis is restricted to the kinematic range $Q^2 > 2500 \text{ GeV}^2$ and $0.1 < y < 0.9$. The resolution in M_e degrades with decreasing y_e ($\delta M_e/M_e \propto 1/y_e$) and so the low y domain is excluded. Excluding the high y values suppresses the photoproduction background (see section 5) and also avoids the region where QED radiative effects are largest for the e -method. For this kinematic range, the NC trigger efficiency exceeds 96% and is consistent with 100% to within experimental error.

Following the NC selection described above, 471 (493) DIS event candidates are accepted using the e -method (2α -method) for the calculation of the kinematic cuts.

3.3 Charged Current Selection and Kinematics

The selection of event candidates for the CC DIS sample requires:

1. the total missing transverse momentum $P_{T,miss} = P_{T,h} > 50 \text{ GeV}$;
2. the total transverse energy $E_T = \sum \sqrt{E_{i,x}^2 + E_{i,y}^2}$ calculated from energy deposits in the calorimeters to match $P_{T,h}$ such that $(E_T - P_{T,h})/E_T < 0.5$.

These cuts eliminate the photoproduction and NC DIS background.

The DIS Lorentz invariants Q^2 , y and M are calculated using the Jacquet-Blondel ansatz [11] by summing over all measured final state hadronic energy deposits using:

$$M_h = \sqrt{\frac{Q_h^2}{y_h}}, \quad Q_h^2 = \frac{P_{T,h}^2}{1 - y_h}, \quad y_h = \frac{\sum (E - P_z)}{2E_e^0}.$$

This method will henceforth be denoted the h -method. The h -method can also be used for NC DIS.

In addition to the cuts (1) and (2) above, the analysis is restricted to the kinematic range $y_h < 0.9$. The resolutions in both M_h and Q_h^2 degrade with increasing y (both $\delta M_h/M_h$ and $\delta Q_h^2/Q_h^2$ behave as $\propto 1/(1 - y_h)$ for $y_h \sim 1$) and so the high y_h domain is excluded. The requirement of cut (1) restricts implicitly the kinematic range to $Q_h^2 > 2500 \text{ GeV}^2$. Throughout this range, the CC trigger efficiency is $\gtrsim 90\%$.

The CC selection described above retains 31 CC DIS event candidates.

4 Standard Model of Deep-Inelastic Scattering

The calculation of an expectation for NC and CC DIS ep scattering is performed using the parton model in the approximation of single γ/Z and W boson exchange. Detailed expressions for the NC and CC cross-sections which contain a description of the proton in terms of scale dependent structure functions can be found in [3]. For NC DIS, the contribution of the longitudinal structure function F_L is neglected. The structure functions are expressed in terms of parton densities which are taken here from the Martin-Roberts-Stirling MRS (H) [12] parametrizations. These were determined by a global fit of structure functions measurements in fixed target experiments [14, 15, 16, 17], inclusive lepton production and direct photon production [18, 19, 20, 21], and low Q^2 structure functions measurements at HERA [22, 23]. The parton densities are evolved to the high Q^2 relevant for this analysis using the next-to-leading order DGLAP equations [24] and divergences are regulated in the DIS renormalization scheme [25]. Higher twist contributions are neglected.

For the comparison with data, a Monte Carlo simulation following such an approach is performed using the event generator DJANGO [26]. This generator includes the QED first order radiative corrections, and emission of real bremsstrahlung photons [27]. Moreover it offers an interface to two possible models for the emission of QCD radiation. The LEPTO [28] model includes the QCD matrix elements to first order in α_s , complemented by leading-log parton showers to model higher order radiation. The ARIADNE [29] generator makes use of the Color Dipole Model [30] to simulate QCD radiation to all orders. Both use string fragmentation [31] to generate the hadronic final state.

A complete Monte Carlo simulation of the H1 detector response is performed for NC and CC DIS processes. For NC DIS, a sample corresponding to $Q^2 > 1000 \text{ GeV}^2$ and which amounts to ~ 25 times the integrated luminosity of the data was produced using ARIADNE. A similar sample was produced using LEPTO. To reduce further the Monte Carlo statistical uncertainty at high Q^2 , a simulation corresponding to ~ 100 times the integrated luminosity of the data was performed using ARIADNE with the additional

requirement $E_e > 50$ GeV on the energy of the scattered positron. The same event generator was used for the simulation of CC DIS events with $Q^2 > 100$ GeV² to give a sample also ~ 100 times the integrated luminosity of the data. For the comparison with experimental data in the following sections, the ARIADNE model for the hadronic final state is used unless explicitly otherwise stated.

The following experimental errors are propagated as systematic errors on the mean standard NC DIS expectation:

- the uncertainty on the integrated luminosity ($\pm 2.3\%$);
- the uncertainty on the absolute calibration of the calorimeters for electromagnetic energies ($\pm 3\%$);
- the uncertainty on the absolute calibration of the calorimeters for hadronic showers ($\pm 4\%$); for NC DIS, this error only enters via the constraints on $P_{T,miss}$ and on $\Sigma(E - P_z)$.

In addition, a 7% “theoretical” uncertainty on the predicted NC DIS cross-section originates from contributions of:

- the uncertainty of 5% on parton density distributions extracted from “QCD fits”; this is partly due to the experimental errors on the input data (in particular in the structure function measurements in the high x range from the BCDMS experiment [14]) and is partly linked to the assumptions for the shapes of the parton distributions at the Q_0^2 at which the perturbative QCD evolution is started; this uncertainty is compatible with what can be inferred from a comparison of the cross-section predictions, calculated with HECTOR [32], using the recent sets of next-to-leading order parametrizations of the MRS [33], CTEQ [34], and GRV [35] groups regulated in the \overline{MS} scheme [36];
- the value of the strong coupling constant α_s , which leads to an uncertainty of 4%; this was inferred by comparing the CTEQ (A1) to (A5) [37] parametrizations with $\alpha_s(M_Z)$ ranging from 0.110 to 0.122; a similar value can be inferred by a comparison of the MRS (R1) and (R2) [33] parametrizations;
- the higher order QED corrections imply a 2% uncertainty in the y range considered in this analysis; this was estimated using HECTOR [32] which makes possible two approaches: QED radiative corrections can be calculated [38] in the leading logarithmic approximation at $\mathcal{O}(\alpha_{em})$ including $\mathcal{O}(\alpha_{em}^2)$ corrections in the next-to-leading logarithmic approximation as well as soft photon exponentiation; alternatively [39], complete QED and electroweak corrections are calculated at $\mathcal{O}(\alpha_{em})$.

All analyses described in the following sections have been repeated with an independent shift of the central values by ± 1 standard deviation of each of the experimental and theoretical sources of errors. The overall systematic error of the standard DIS model prediction is determined as the quadratic sum of the resulting errors and of the statistical error on the Monte Carlo simulation.

5 Background Sources

The contributions from background processes which could give rise to events with true or misidentified isolated positrons at high E_T or to events with a large $P_{T,miss}$ were evaluated using the full simulation and reconstruction program chain. The list of processes is given in Table 1.

The production of real electroweak vector bosons Z^0 and W^\pm was modelled using the EPVEC event generator [40]. This includes processes where the partonic structure of a photon is resolved. It should be noted that inelastic single Z^0 and W^\pm production is not contained in the standard DIS model described in section 4 and thus it is treated here as a background source. Especially contributions from radiation of a Z^0 or W^\pm from a quark can give rise to forward positrons and thus can mimic NC DIS events at very high Q^2 .

Direct and resolved photoproduction processes were modelled using the PYTHIA generator [41]. It is based on leading order QCD matrix elements and includes initial and final state parton showers calculated in the leading logarithm approximation, and string fragmentation [31]. To enhance the generated yield of events in the hard scattering region, the transverse momenta \hat{p}_T in the hard sub-processes are required to exceed 10 GeV for light quark flavour production, 3 GeV for prompt photon processes, and 8 GeV for heavy quark flavour production. These cuts do not affect the production of jets with $P_T > 25$ GeV (or of jets containing hard fragments with $\sum_{e,\gamma} P_T > 20$ GeV), or the production of prompt photons with $P_T > 10$ GeV. The renormalization and factorization scales are both set to P_T^2 . The GRV (G) leading order parton densities in the photon are used [42].

Contributions from two-photon ($\gamma\gamma$) processes, where one γ originates from the proton, were also considered. Electron-positron pair production $e^+p \rightarrow e^+ + e^+e^- + X$, where at least one of the leptons has high P_T , was simulated using the LPAIR generator [43]. LPAIR includes the relevant Bethe-Heitler diagrams to lowest order in α_{em} (i.e. order α_{em}^4) but does not include the photon bremsstrahlung diagrams where the photon converts into a lepton pair or any diagrams in which real or virtual photons are replaced by Z^0 bosons. The contribution from $q\bar{q}$ production in $\gamma\gamma$ collisions was simulated using PYTHIA [41] by folding in appropriate γ fluxes [44], and it did not include diagrams involving massive electroweak bosons. The diagrams for both final states (e^+e^- and $q\bar{q}$) which involve the formation of a Z^0 vector boson are included in the calculations of electroweak vector boson production using the EPVEC generator.

When the high Q^2 DIS selection criteria which are described in section 3 are applied to the above background sources, the total remaining background contamination is found to be below 1% (95% CL). Nevertheless, in order to ensure that the background contamination is negligible everywhere in the kinematic plane compared with the uncertainty on the standard DIS expectation, additional cuts are imposed. Each cut is specifically designed to eliminate a given background source.

Background contamination in the NC DIS selection is suppressed by the following:

1. processes leading to multi-lepton final states are eliminated by requiring at least one reconstructed jet with $E_{T,jet} > 7$ GeV in the polar angular range $10^\circ \leq \theta_{jet} \leq 145^\circ$;

Partonic Process (example)	Generator Model [refs.]	Simulated Luminosity (pb ⁻¹)	Upper Limits (95% CL) on Events per 14.19 pb ⁻¹
Single W and Z Boson Production			
$e + q \longrightarrow W + e + X$ $\hookrightarrow e + \nu$ $\hookrightarrow \text{jet} + \text{jet}$	[40]	8600 1400	0.005 0.16
$e + q \longrightarrow Z + e + X$ $\hookrightarrow e^+ + e^-$ $\hookrightarrow \tau^+ + \tau^-$ $\hookrightarrow \text{jet} + \text{jet}$	[40]	42000 59000 3600	0.003 0.001 0.18
High P_T jets photoproduction (direct and resolved)			
$\gamma + q \rightarrow q + g, \gamma + g \rightarrow q + \bar{q}'$ (hard jet)	[41]	500	0.38
(hard fragmentation)		500	0.31
Heavy Flavour Production (direct and resolved)			
$\gamma + g \longrightarrow c + \bar{c}$ $\gamma + g \longrightarrow b + \bar{b}$	[41]	600 600	0.07 0.07
Prompt Photon Production (direct and resolved)			
$\gamma + q \rightarrow q + \gamma$	[41]	500	0.09
Two-photon processes			
$\gamma + \gamma \longrightarrow e^+ + e^-$ $\gamma + \gamma \longrightarrow q + \bar{q}$	[43]	4500 17000	0.04 0.002

Table 1: Upper limits (95% CL) on the expected number of events from background processes which survive the event selection for NC DIS candidates and the full set of background rejection cuts; for the photoproduction of high P_T jets involving light quark flavours, two alternative selections are made which require either a hard jet or jets containing hard leptons, photons or π^0 's.

the jet is specified using a cone algorithm with a radius $\sqrt{\Delta\eta_{jet}^2 + \Delta\phi_{jet}^2} = 1$; at least 1% of the jet energy should be deposited in the hadronic section of the LAr calorimeter;

2. QED Compton events are suppressed by rejecting events in which a second positron (or photon) cluster with $E_{T,e(2)}/E_{T,e} > 0.9$ is found back-to-back in azimuth within $\Delta\phi_{e,2} > 160^\circ$;
3. background from single Z^0 boson production followed by a $Z^0 \rightarrow e^+e^-$ decay is suppressed by rejecting events in which the invariant mass of two electron/positron clusters lies within 5 GeV of the Z^0 boson mass;
4. background from single Z^0 boson production followed by a $Z^0 \rightarrow \tau^+\tau^-$ decay is

eliminated by the requirement $\sum (E - P_z) > 0.2 \times P_{T,miss} + 43 \text{ GeV}$, which rejects events having both abnormally high $P_{T,miss}$ and abnormally low $\sum (E - P_z)$;

5. background from isolated prompt photons in photoproduction processes is eliminated by requiring that there be at least one charged track within the positron isolation cone;
6. background from photoproduction and low Q^2 NC DIS are removed by the requirement that there be less than 5 GeV in the backward calorimeters; moreover there should be no energy E_{e-tag} in the e -tagger, unless $|E_{e-tag} + E_{\gamma-tag} - E_e^0| < 5 \text{ GeV}$, where $E_{\gamma-tag}$ is the energy in the γ -tagger, in order to save NC DIS events which coincide randomly with Bethe-Heitler bremsstrahlung;
7. background from e^+e^- pair production in γ - γ collisions is strongly suppressed by requiring that there be in addition to the “scattered” positron at most one electron/positron candidate with $E_T > 4 \text{ GeV}$.

The cuts (2), (3), (4), (5) and (7) each imply individually an efficiency loss for NC DIS processes below 1% while the corresponding losses for cuts (1) and (6) are below 2%. Globally, the complete set of background rejection cuts leads to a 5% efficiency loss for NC DIS. It should be noted that the background originating from single Z^0 or W^\pm production followed by hadronic decay of the boson, and leading to multi-jet final states, could be considerably reduced by requiring that at most one jet carries $E_{T,jet} > 40\% E_{T,e}$. This requirement has not been imposed in this analysis in order to stay as close as possible to an inclusive DIS measurement. Applying all selection cuts and background rejection cuts, the remaining background contamination is below 0.1% (95% CL) for the NC DIS sample. Hence, the background is negligible when compared to the estimated errors on the standard NC DIS expectation. This statement is also valid in a restricted kinematic range of $Q^2 > 10000 \text{ GeV}^2$ where less than 0.1 (95% CL) background events are expected. In most cases, the estimation of upper limits for the various background sources in Table 1 are limited by available Monte Carlo statistics.

To deal with specific background sources to CC DIS, it is required that there should be no isolated positron with $E_{T,e} > 10 \text{ GeV}$ within $10^\circ \leq \theta_e \leq 145^\circ$. This rejects in particular background from single W boson production followed by a $W \rightarrow e\nu$ decay. This causes negligible efficiency losses for the CC DIS selection, while the remaining contamination from single W production is below 0.02% (95% CL) within the analysis cuts.

The purity of the event selection is cross-checked by two methods:

1. for the NC selection, the positron isolation criteria were relaxed and the positron cluster to charged track link was not applied; no evidence for background was found;
2. all events from the NC and CC selection were scanned visually; in the selected NC sample, no contamination or overlap with cosmic ray showers or beam halo events was seen; there was no evidence for wrongly identified positron clusters; the selected CC sample showed no sign of contamination due to cosmic ray showers; no muon candidate was found in any of the selected events.

6 Analysis

6.1 General Properties of NC and CC Events

The measured data are compared with the expectation from the standard DIS model. Here and in all that follows, the expected yields of events are calculated using Monte Carlo simulation of the H1 detector response, including all detector and selection efficiencies, and the full H1 event reconstruction program. All comparisons with measurement are made with a normalization specified by the total cross-section within acceptance and the measured integrated luminosity.

We find in the experimental data 443 (460) NC DIS candidates satisfying the selection criteria and $Q_e^2 > 2500 \text{ GeV}^2$ ($Q_{2\alpha}^2 > 2500 \text{ GeV}^2$), which is in good agreement with the expectation of 427 ± 38 (442 ± 40) from NC DIS processes. Within the kinematic range in θ_e , $E_{T,e}$, y_e and Q_e^2 considered, the ratio of this expected number of events to the number generated by the Monte Carlo simulation is about 0.8 due to experimental acceptance and event selection. The sources of errors for the NC DIS expectation are discussed above. For the CC DIS candidates, 31 events are found satisfying the above requirements,

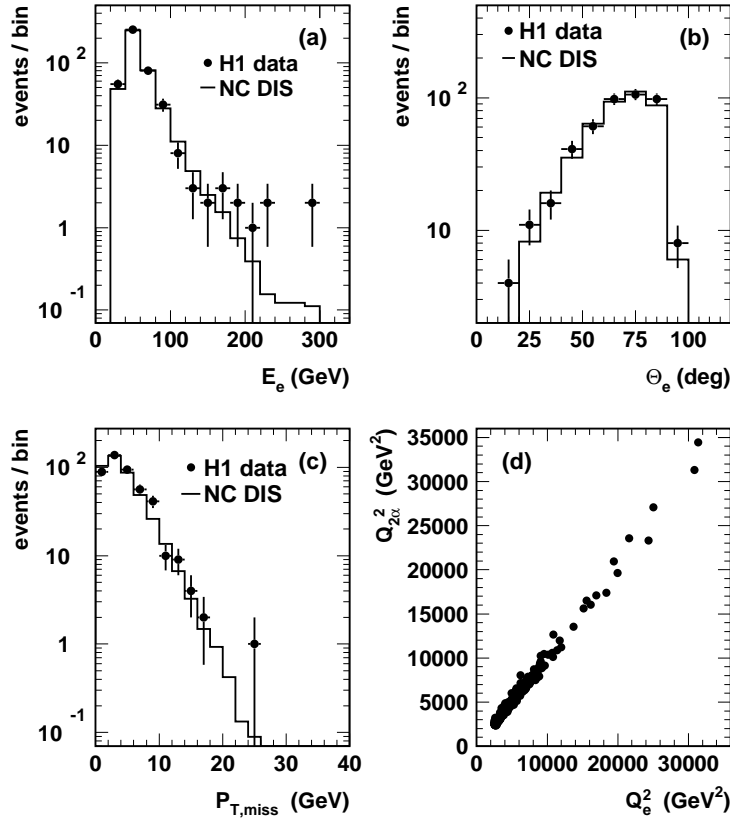


Figure 1: For NC DIS candidates, the distributions of (a) the measured positron energy E_e , (b) the polar angle θ_e , (c) the missing transverse momentum $P_{T,miss}$, and (d) the correlation of $Q_{2\alpha}^2$ and Q_e^2 , (symbols); in (a), (b) and (c) the expectations from standard NC DIS assuming the integrated luminosity of the measurement are shown as superimposed histograms.

which agrees well with the expectation of 34.2 ± 5.8 from CC DIS processes. Here the corresponding ratio of accepted to generated events is again about 0.8 in the $P_{T,miss}$ and y_h range considered.

Fig. 1 shows, for NC DIS candidates, the distributions of energy and polar angle of the scattered positron, the missing transverse momentum, and the correlation of the 4-momentum transfer squared Q^2 calculated with the e -method (Q_e^2) and the 2α -method ($Q_{2\alpha}^2$). Superimposed as histograms are the expectations from the NC DIS simulation. The distributions are well described by the simulation except for the largest values of the measured positron energy E_e . This will be quantified below in terms of Q^2 to which E_e is closely related at large values. A good correlation is seen between the measurement of Q^2 by the electron and the 2α -method.

Fig. 2 shows the measured and expected differences between various mass reconstruction methods. The e -method, which provides good resolution for all kinematic quantities

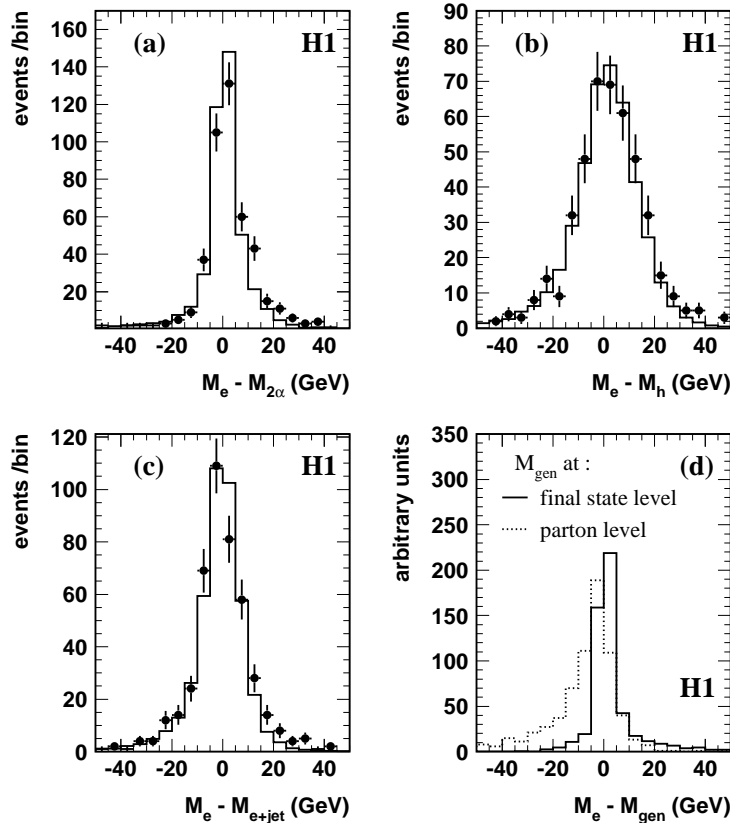


Figure 2: Distributions for the NC DIS sample of the differences between the mass ($M = \sqrt{xs}$) calculated using the e -method (M_e) and (a) using the 2α -method ($M_{2\alpha}$), (b) using the h -method (M_h), and (c) using the invariant mass of the positron-jet system (M_{e+jet}); superimposed on the data points (\bullet symbols) are histograms of the expectation from the Monte Carlo simulation; (d) difference between M_e and the generated mass M_{gen} when the latter is calculated either from the final state positron using simulated NC DIS events (histogram), or taken from the invariant mass of the positron-quark sub-system in a specific eq resonance model (dotted histogram).

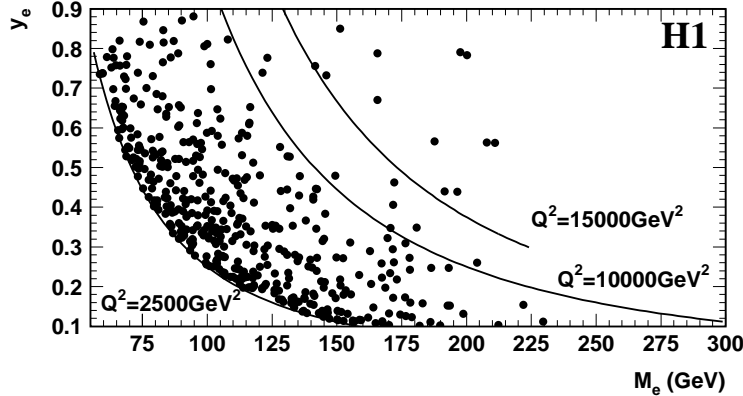


Figure 3: Selected NC DIS candidate events in the $M_e - y_e$ plane; three contours of fixed Q^2 are shown.

at $y_e > 0.1$, is taken here as a reference. Good agreement is found between the mass measurement M_e based on the e -method and $M_{2\alpha}$ based on the 2α -method (Fig. 2a). The difference $M_e - M_{2\alpha}$ is found to be described acceptably by the NC DIS simulation. The measurement M_e is compared to M_h calculated from the hadronic energy flow in Fig. 2b. Also here good agreement is found between the two methods and the shape of the $M_e - M_h$ distribution is well described by the simulation. This confirms the validity of the h -method which is the only one available to reconstruct the kinematics of CC DIS events. A comparison of M_e with the invariant mass M_{e+jet} calculated from the energies and angles of the final state positron and highest E_T jet is shown in Fig. 2c. Good agreement is found between the two mass methods which reflects the fact that the measurement is dominated by hard $e + parton \rightarrow e + parton$ scattering leading most often to a hadronic final state with a single high transverse energy jet. Also the difference $M_e - M_{e+jet}$ is well described by the simulation.

Fig. 2d shows the expected experimental contribution to the resolution on M_e obtained by comparing for the NC DIS simulation the reconstructed and generated positron momentum 4-vectors. The mean value of the distribution of the reconstructed M_e is within $\pm 1\%$ of the true value of the Lorentz invariant $M = \sqrt{xs}$ calculated from the generated final state positron for the range of y considered. With respect to this generated positron, values of M_e are measured with an RMS resolution of $\sigma_{RMS} \simeq 7$ GeV and a Gaussian peak resolution of $\sigma_{Gauss} \simeq 3.0$ GeV. Also shown as a dotted histogram is the expected resolution of the e -method for the invariant mass of the positron-parton system in a specific model (see section 7). It should be recalled that the M_e resolution severely degrades at low y_e and the events in Fig. 2 are restricted to $y_e > 0.1$. A shift equal to the experimental systematic error on the calorimeter energy scale for positrons of 3% would lead to a y dependent shift for the mass M_e of $\delta M_e/M_e = 0.03/(2y_e)$.

Fig. 3 shows the two dimensional distribution of y_e against M_e . The cut-off in event density for low y_e or M_e arises because of the requirement $Q_e^2 > 2500$ GeV². Also shown are the $Q_e^2 = 10000$ GeV² and $Q_e^2 = 15000$ GeV² contours.

Fig. 4a and 4b show the projected M_e and y_e distributions of the selected events at

“low” Q^2 ($2500 \text{ GeV}^2 < Q_e^2 < 15000 \text{ GeV}^2$) and Fig. 4c and 4d at “high” Q^2 ($Q_e^2 > 15000 \text{ GeV}^2$). The distributions of the data are well reproduced by standard DIS predictions in the low Q^2 range. At high Q^2 the data exceed the NC DIS expectation, especially

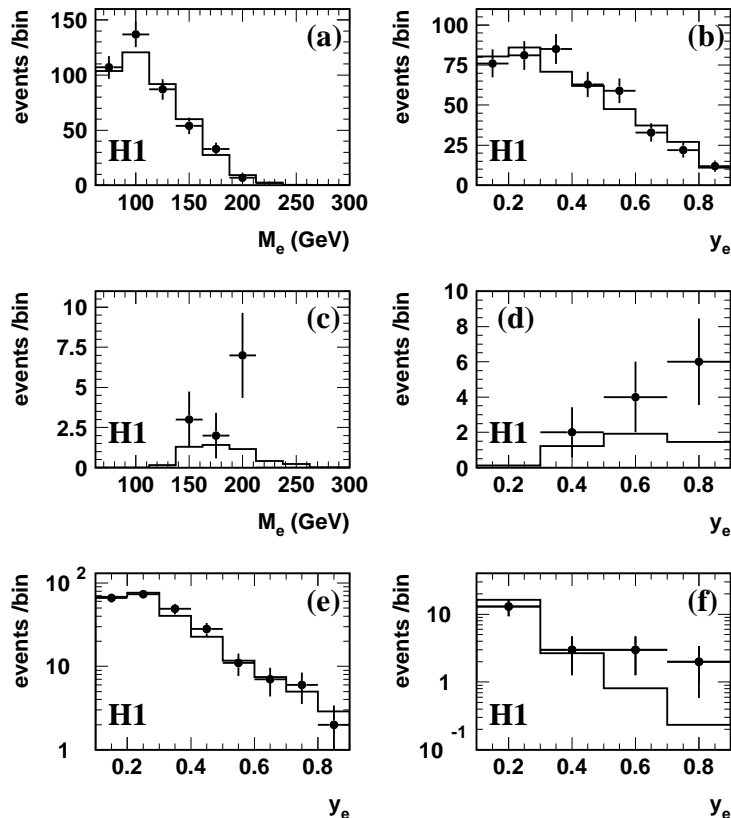


Figure 4: Distributions of M_e and y_e for selected NC DIS candidate events, (a) and (b) for $2500 \text{ GeV}^2 < Q_e^2 < 15000 \text{ GeV}^2$, (c) and (d) for $Q_e^2 > 15000 \text{ GeV}^2$; distribution of y_e (e) for $100 < M_e < 180 \text{ GeV}$ and (f) for $M_e > 180 \text{ GeV}$; superimposed on the data points (\bullet symbols) are histograms of the expectation of standard NC DIS.

at $M_e \sim 200 \text{ GeV}$. Fig. 4e and 4f show the y_e distributions for M_e values below and above 180 GeV . At high M_e , a difference between experiment and expectation is apparent at large y_e .

6.2 Q^2 Dependence

6.2.1 Neutral Current Sample

Fig. 5 shows for the NC selection the measured Q_e^2 distribution in comparison with the expectation from standard NC DIS processes. Also shown is the ratio of the Q_e^2 distribution to the NC DIS expectation. Very similar results are obtained for this ratio for minimum values of y_{min} in the range 0.1 to 0.5 . The errors resulting from the convolution of the statistical error of the Monte Carlo sample and the systematic errors are correlated

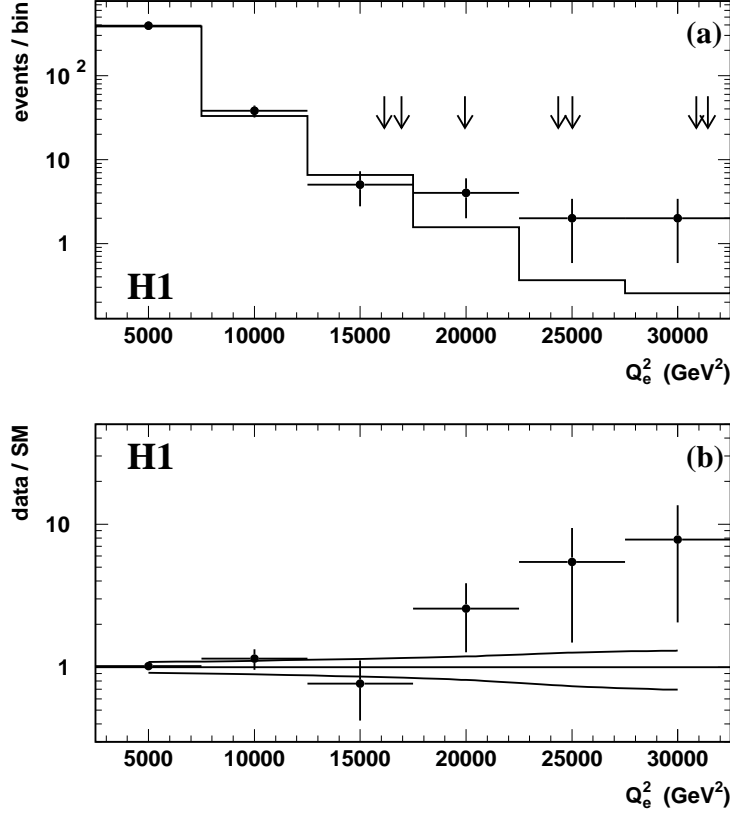


Figure 5: (a) Q_e^2 distribution of the selected NC DIS candidate events for the data (\bullet symbols) and for standard NC DIS expectation (histogram); the arrows indicate the Q_e^2 values for data entries with $Q_e^2 > 15000 \text{ GeV}^2$ and $M_e > 180 \text{ GeV}$; (b) ratio of the observed and expected number of events as a function of Q_e^2 ; the lines above and below unity specify the $\pm 1\sigma$ levels determined using the combination of statistical and systematic errors of the NC DIS expectation.

for different Q_e^2 bins and are indicated in Fig. 5b. They are shown in this figure (and in subsequent figures 6 and 7) as lines above and below unity joining the $\pm 1\sigma$ errors evaluated at the center of each bin. These errors are dominated by the uncertainty in the electromagnetic energy scale of the calorimeter and vary between 8.5% at low Q_e^2 and 30% at the highest values of Q_e^2 . The NC DIS expectation agrees well with the data for $Q_e^2 \lesssim 15000 \text{ GeV}^2$ while at larger Q_e^2 the number of events is in excess of the NC DIS expectation.

To quantify this difference, the numbers of observed and expected events with Q_e^2 above various Q_{min}^2 values are given in Table 2. Also given in Table 2 are the Poisson probabilities $\mathcal{P}(N \geq N_{obs})$ that in a random set of experiments the number of NC DIS events N fluctuates to values equal to or larger than the observed number of events N_{obs} . The systematic error δb on the mean number of expected events b is taken into account

Q_{min}^2 (GeV ²)	2500	5000	10000	15000	20000	30000
N_{obs}	443	122	20	12	5	2
N_{DIS}	426.7 ±38.4	116.2 ±11.6	18.3 ±2.4	4.71 ±0.76	1.32 ±0.27	0.23 ±0.05
$\mathcal{P}(N \geq N_{obs})$	0.35	0.35	0.39	6×10^{-3}	1.4×10^{-2}	2.3×10^{-2}

Table 2: Number of observed (N_{obs}) and expected NC DIS (N_{DIS}) events with 4-momentum transfer squared Q_e^2 above given thresholds (Q_{min}^2); $\mathcal{P}(N \geq N_{obs})$ is the probability that the number of NC DIS events fluctuates to values equal to or larger than N_{obs} in a random set of experiments.

by using the convolution :

$$\mathcal{P}(N \geq N_{obs}) = \int_0^{+\infty} dx G(x; b, \delta b) \sum_{k=N_{obs}}^{\infty} p(k; x)$$

where the following notations have been introduced :

- $p(k; x)$ is the Poisson probability to observe k events when the number of expected events is x , i.e. $p(k; x) = e^{-x} x^k / k!$;
- $G(x; b, \delta b)$ is the probability density function for the NC DIS expectation x , namely a Gaussian of mean value b and width δb .

The resulting probabilities are about 1% at the largest Q_{min}^2 values. For $Q^2 > 15000$ GeV², the number of observed events is $N_{obs} = 12$ for an expectation of 4.71 ± 0.76 corresponding to a probability $\mathcal{P}(N \geq N_{obs})$ of 6×10^{-3} .

6.2.2 Charged Current Sample

Fig. 6 shows for the CC selection the measured Q_h^2 distribution in comparison with the standard DIS CC expectation. The systematic errors are relatively large and dominated

Q_{min}^2 (GeV ²)	2500	5000	10000	15000	20000
N_{obs}	31	24	10	4	3
N_{DIS}	34.2 ±5.8	21.1 ±4.2	5.07 ±1.88	1.77 ±0.87	0.74 ±0.39
$\mathcal{P}(N \geq N_{obs})$	0.64	0.31	7×10^{-2}	0.14	5.4×10^{-2}

Table 3: Number of observed (N_{obs}) and expected CC DIS events (N_{DIS}) with 4-momentum transfer squared Q^2 above given Q_{min}^2 values; $\mathcal{P}(N \geq N_{obs})$ is the probability that the number of CC DIS events fluctuates to values equal to or larger than N_{obs} in a random set of experiments.

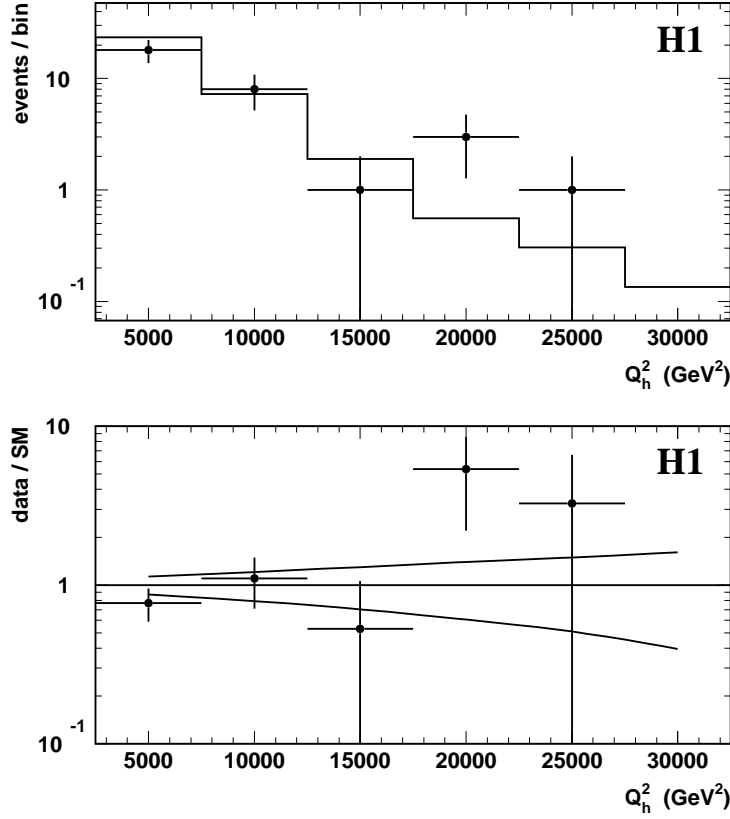


Figure 6: (a) Q_h^2 distribution of the selected CC DIS candidate events for the data (\bullet symbols) and for standard CC DIS expectation (histogram); (b) ratio of the observed and expected number of events as a function of Q_h^2 ; the lines above and below unity specify the $\pm 1\sigma$ levels determined using the combination of statistical and systematic errors of the CC DIS expectation.

by the uncertainty on the hadronic energy scale of the calorimeter. They vary between 12% at $Q_h^2 \simeq 5000 \text{ GeV}^2$ and 60% at $Q_h^2 \simeq 30000 \text{ GeV}^2$. Within errors, the distribution of the measured events is reproduced both in shape and in absolute normalization. Table 3 gives the number of observed and expected CC events, as well as the Poisson probability $\mathcal{P}(N \geq N_{obs})$ as defined in section 6.2.1, for increasing values of Q_{min}^2 . In the kinematic region $Q_h^2 > 15000 \text{ GeV}^2$, there are $N_{obs} = 4$ observed events compared with an expectation of 1.77 ± 0.87 from standard CC DIS. This small difference corresponds to a Poisson probability $\mathcal{P}(N \geq N_{obs})$ of 14%, including systematic errors, that the CC DIS signal fluctuates to values equal to or larger than N_{obs} in a random set of experiments.

6.3 Mass Dependence as a Function of y

Fig. 7a shows the measured and expected M_e distribution and Fig. 7b the ratio of the measured M_e distribution to NC DIS expectation for a minimum y_e value of $y_{min} = 0.2$. Similar distributions are shown in Fig. 7c and 7d for $y_{min} = 0.4$. An excess of events over the NC DIS expectation at the highest mass ($\sim 200 \text{ GeV}$) is seen, which becomes more

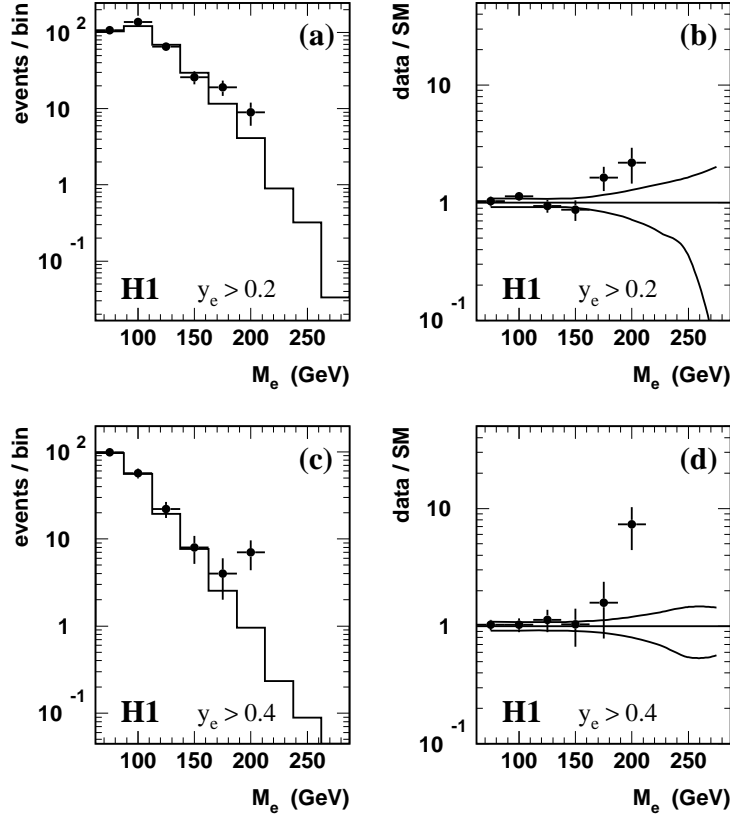


Figure 7: (a) Distribution of M_e for the observed (\bullet symbols) NC DIS candidates with $y_e > 0.2$; the expectation from standard NC DIS is shown as the superimposed histogram; (b) ratio of the observed and expected numbers of events as a function of M_e for $y_e > 0.2$; the lines above and below unity specify the $\pm 1\sigma$ levels of uncertainty for the standard NC DIS expectation using the combination of statistical and systematic errors; (c) as in (a) but now with $y_e > 0.4$; (d) as in (b) but now with $y_e > 0.4$.

visible with the larger y_{min} cut.

To quantify the difference in the M_e distribution between the data and the expectation, the number of events with M_e and y_e above various sets of minimal values M_{min} and y_{min} are given in Table 4. Also given are the Poisson probabilities $\mathcal{P}(N \geq N_{obs})$ that the standard NC DIS signal N fluctuates to values equal to or larger than the number of observed events in a random set of experiments. The errors on the NC expectation as well as the probabilities take into account all systematic errors described in section 4. It is noted that the values obtained for the various sets of M_{min} and y_{min} cuts are correlated. Good agreement is observed for low M_{min} and y_{min} , whereas at high M_{min} and y_{min} the probabilities $\mathcal{P}(N \geq N_{obs})$ become smaller.

The range of M_e values for which the most significant excess over NC DIS expectation exists is investigated in detail by considering “windows” of various total widths ΔM_e . The central values M_e of the mass windows are varied in steps of 1 GeV between 80 and

M_{min} (GeV) \ y_{min}	0.2	0.3	0.4	0.5	
75	N_{obs}	313	232	147	84
	N_{DIS}	294.1 ± 26.2	208.1 ± 16.9	136.9 ± 11.2	77.1 ± 5.9
	\mathcal{P}	0.27	0.14	0.26	0.25
150	N_{obs}	34	17	12	8
	N_{DIS}	28.0 ± 4.6	12.9 ± 1.6	6.83 ± 0.80	3.51 ± 0.40
	\mathcal{P}	0.19	0.18	5.3×10^{-2}	3.0×10^{-2}
175	N_{obs}	14	9	7	5
	N_{DIS}	9.82 ± 2.62	4.65 ± 0.77	2.35 ± 0.38	1.31 ± 0.21
	\mathcal{P}	0.18	5.8×10^{-2}	1.3×10^{-2}	1.2×10^{-2}
180	N_{obs}	11	8	7	5
	N_{DIS}	7.85 ± 2.35	3.73 ± 0.70	1.83 ± 0.33	1.04 ± 0.17
	\mathcal{P}	0.22	4.6×10^{-2}	3.8×10^{-3}	5.0×10^{-3}
185	N_{obs}	10	7	7	5
	N_{DIS}	6.10 ± 2.06	2.89 ± 0.57	1.41 ± 0.26	0.83 ± 0.15
	\mathcal{P}	0.14	3.6×10^{-2}	9.4×10^{-4}	2.0×10^{-3}
190	N_{obs}	8	6	6	4
	N_{DIS}	4.65 ± 1.68	2.19 ± 0.48	1.07 ± 0.23	0.68 ± 0.13
	\mathcal{P}	0.15	3.1×10^{-2}	1.2×10^{-3}	5.9×10^{-3}
195	N_{obs}	6	5	5	4
	N_{DIS}	3.58 ± 1.43	1.73 ± 0.40	0.85 ± 0.19	0.53 ± 0.11
	\mathcal{P}	0.19	3.8×10^{-2}	2.4×10^{-3}	2.5×10^{-3}
200	N_{obs}	4	3	3	3
	N_{DIS}	2.72 ± 1.10	1.32 ± 0.33	0.63 ± 0.15	0.39 ± 0.09
	\mathcal{P}	0.30	0.15	2.8×10^{-2}	8.2×10^{-3}

Table 4: Numbers of observed (N_{obs}) NC DIS candidates and expected (N_{DIS}) standard NC DIS events which satisfy the NC DIS selection for different minimal requirements $y_e \geq y_{min}$ and $M_e \geq M_{min}$; also given is the probability $\mathcal{P} = \mathcal{P}(N \geq N_{obs})$ that the number of DIS events fluctuates to values equal to or larger than N_{obs} in a random set of experiments.

250 GeV and the numbers of observed and expected events are determined for different y_{min} values. For each mass window, the Poisson probability $\mathcal{P}(N \geq N_{obs})$ is determined, including the propagation of all systematic errors described above. The probability for each value of M_e reflects the level of agreement between data and expectation for an *a priori* choice of M_e . To avoid the inevitable discontinuities when values of \mathcal{P} are displayed due to the small number of observed events, a probability $\bar{\mathcal{P}}$ is calculated averaging over 3 steps of 1 GeV around the given central M_e value. The resulting Poisson probabilities as a function of the central value M_e are shown in Fig. 8 for a representative choice of ΔM_e and y_{min} settings. This 3 GeV range corresponds to the M_e spread due to the finite resolution on the measurement of the scattered positron energy (see Fig. 2d).

For low y_{min} , the probabilities fluctuate statistically as expected. At masses above ~ 220 GeV no data event is observed within the mass windows, and the probabilities $\bar{\mathcal{P}}(N \geq N_{obs})$ approach unity by construction. There remain ~ 0.3 NC DIS events expected in

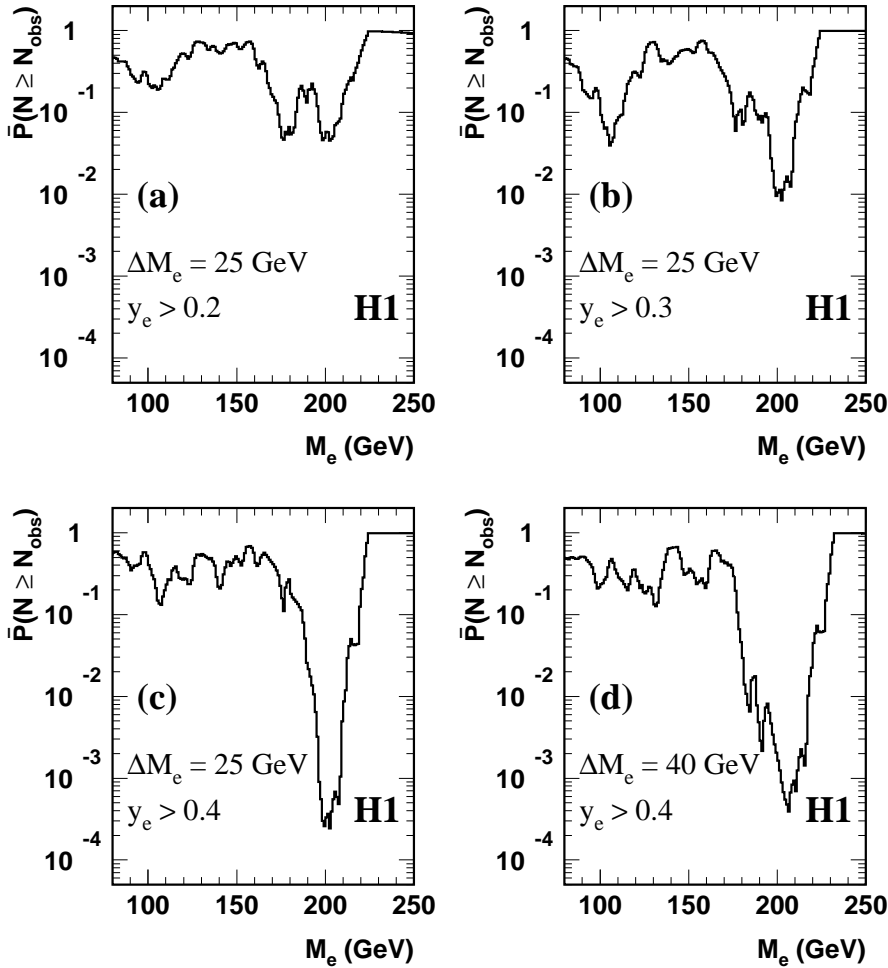


Figure 8: Probability that the standard NC DIS signal fluctuates to values equal to or larger than the number of observed events in a random set of experiments for various y_{min} values. The probability is calculated for different sliding mass windows of widths ΔM_e and averaged over 3 steps of 1 GeV. At the highest masses, where no data events are observed, the probabilities approach unity by construction.

this high mass region for $y_{min} = 0.4$. For y_{min} values of 0.3 and 0.4 and for a window width varying between 25 and 40 GeV, the lowest probabilities of 10^{-2} to 2.6×10^{-4} are observed for a central mass value $M_e \sim 200$ GeV. For $y_{min} \sim 0.4$, the probabilities are below 8×10^{-4} for $\Delta M_e = 25$ GeV and central M_e values chosen *a priori* in the range ~ 198 GeV to ~ 208 GeV. This statement holds with or without averaging \mathcal{P} over up to 5 steps of 1 GeV. It should be noted that the systematic error on the energy calibration, which implies an uncertainty on the number of expected NC DIS events and is taken into account in the statistical calculations, gives rise to an uncertainty of approximately ± 5 GeV for the position of the minima in Fig. 8. The results obtained for a fixed central mass value of 200 GeV with $y_{min} = 0.4$ and for various choices of ΔM_e , are given in Table 5.

In order to estimate the likeliness that in a random experiment a value of $\bar{\mathcal{P}}$ smaller

ΔM_e (GeV)	20	25	30	40
N_{obs}	5	7	7	7
N_{DIS}	0.63 ± 0.13	0.95 ± 0.18	1.10 ± 0.19	1.57 ± 0.28
$\bar{\mathcal{P}}(N \geq N_{obs})$	5.0×10^{-4}	2.6×10^{-4}	2.5×10^{-4}	1.6×10^{-3}

Table 5: Number of observed NC DIS candidates (N_{obs}) and expected standard NC DIS events (N_{DIS}) for different mass windows of total width ΔM_e , an *a priori* choice for the central mass value of 200 GeV and for $y_e > 0.4$; also given are the probabilities $\bar{\mathcal{P}}(N \geq N_{obs})$ as defined for Fig. 8.

than the observed probabilities is obtained anywhere in the mass range from 80 to 250 GeV, a large number of Monte Carlo experiments were performed. For each of these experiments, events were randomly chosen according to the NC DIS expectation. The mean number of events in these experiments was conservatively taken to be equal to the number of observed events in the corresponding M_e and y_e range. Applying the same sliding mass procedure as used above for the real experiment and comparing with NC DIS expectation including error propagation, less than 1% of all Monte Carlo experiments yielded a minimum value $\bar{\mathcal{P}}$ below those obtained in Fig. 8c and 8d.

6.4 The Events at Very High Q^2 , M and y

We find 7 events in the kinematic region $M > 180$ GeV and $y > 0.4$ compared with an expectation from NC DIS of 1.83 ± 0.33 (1.75 ± 0.32) using the e -method (2α -method) These events are largely responsible for the excess of observed events over standard DIS expectation in the Q^2 , M and y distributions in Fig. 4, 5 and 7. They are listed in Table 6 and their properties are discussed here in more detail. One of these events is displayed in Fig. 9.

For most of these events, the positron is well contained within the fiducial volume of the LAr calorimeter. The corrections for material in front of or in between calorimeter modules, which are applied during the reconstruction of the energy from showers in the calorimeter, were found to be less than 1% (9%) except for the electromagnetic (hadronic) showers of events 3 and 6 (6). The electromagnetic showers initiated by the positron of events 3 and 6 are corrected by 23% and 5% respectively because they develop near a projective azimuthal edge of a calorimeter module. The corrections to the energy of the hadronic showers of event 6 is 29% also largely due to shower leakage into dead material in between calorimeter modules. The agreement between the different estimators of the kinematic variables in Table 6 demonstrates that the corrections are well understood on average. In particular, the two estimators M_e and $M_{2\alpha}$ are seen to agree well with each other and also with the invariant mass M_{e+jet} calculated from the positron and the highest E_T jet in the final state.

In each event, the identified positron cluster is geometrically linked to at least one

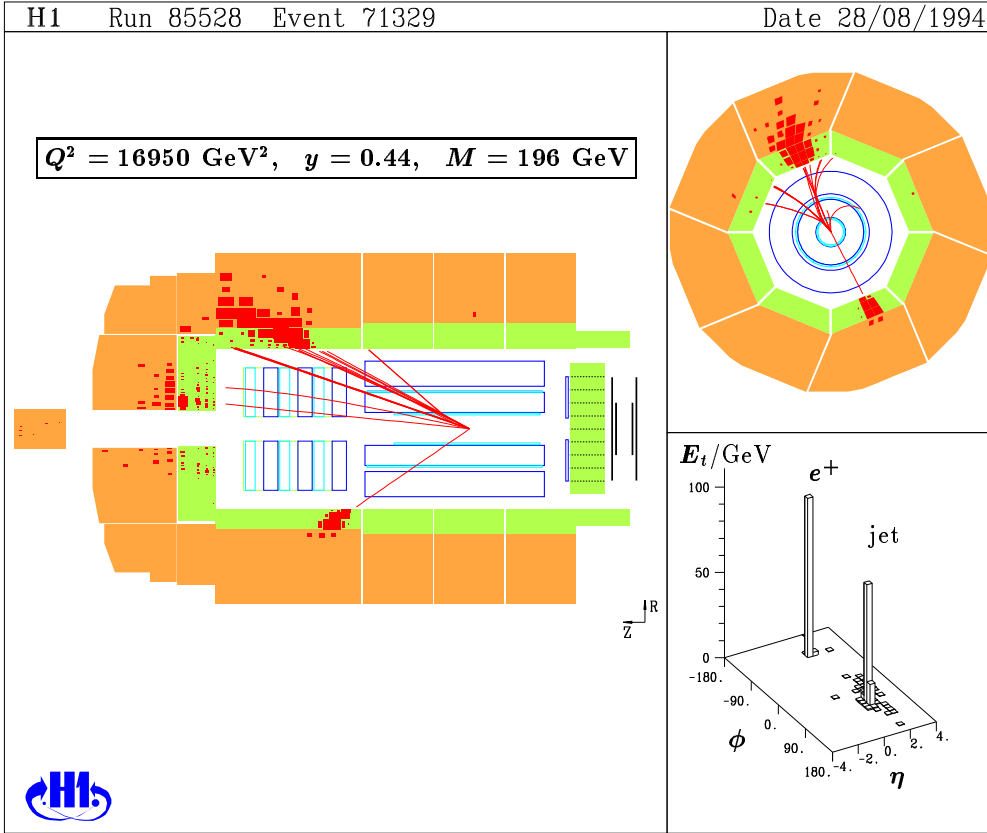


Figure 9: An event of the NC DIS sample at $M_e > 180 \text{ GeV}$ and $y_e > 0.4$.

high momentum charged track. In one case (event 4), multiple tracks or track segments are associated spatially with the positron cluster as expected from Monte Carlo studies in $15 \pm 5\%$ of events with similar kinematics, given the inactive material between the calorimeter and the ep interaction vertex. The 7 events are not confined to any particular azimuthal region of the detector. One event (5) is found to have 2.9 GeV deposited in the photon detector used to determine luminosity from Bethe-Heitler interactions. The probability that one event out of seven of the high Q^2 , high y sample be in random coincidence with an elastic Bethe-Heitler interaction with one photon detected is estimated to be $\sim 35\%$. None of the 7 events have high momentum muons which penetrate the calorimeter and instrumented iron filter. For each of the 7 events, only one jet is found with $E_{T,jet} > 15 \text{ GeV}$ with the cone algorithm and this jet carries more than 90% of the transverse hadronic energy flow.

All the above indicate that these 7 events are well measured NC DIS-like candidates. From Table 6, the weighted average mass $\langle M_e \rangle$ measured for these candidates is $200.8 \pm 2.2 \text{ GeV}$. This value does not include the systematic uncertainty of 3% associated with the absolute energy scale of the electromagnetic calorimeter. This uncertainty leads to a correlated error for all events which depends on y_e like $\delta M_e/M_e = 0.03/(2y_e)$, $\delta y_e = 0.03(y_e - 1)$ and $\delta Q_e^2/Q_e^2 = 0.03$.

For the CC DIS sample, in the kinematic region $Q_h^2 > 15000 \text{ GeV}^2$, which includes the region in which an excess is observed in NC DIS, there are $N_{obs} = 4$ events in agreement

	Run # Event #	M_e (GeV)	$M_{2\alpha}$ (GeV)	M_{e+jet} (GeV)	y_e	$y_{2\alpha}$	Q_e^2 (GeV ²)	$Q_{2\alpha}^2$ (GeV ²)
1	85528	196	198	195	.439	.434	16950	17100
	71329	± 5			± 0.014		± 360	
2	87050	208	200	213	.563	.582	24350	23320
	8062	± 4			± 0.012		± 430	
3	88999	188	185	184	.566	.573	19950	19640
	106218	± 12			± 0.032		± 1400	
4	119314	198	199	197	.790	.787	30870	31320
	18272	± 2			± 0.008		± 530	
5	122145	211	227	211	.562	.526	25030	27100
	69506	± 4			± 0.012		± 440	
6	155768	192	190	215	.440	.443	16130	16050
	67216	± 6			± 0.016		± 400	
7	158577	200	213	210	.783	.762	31420	34450
	100110	± 2			± 0.008		± 540	

Table 6: NC DIS candidates satisfying the kinematic requirement $M > 180$ GeV and $y > 0.4$ when M and y are calculated with either the e -method or the 2α -method; the errors given for the e -method take into account the energy and angular resolution for the positron, and a 30% uncertainty assigned to dead material corrections; the systematic uncertainty of 3% associated with the absolute energy scale of the electromagnetic calorimeter (see text) is not included.

with the expectation of 1.77 ± 0.87 from standard CC DIS. These 4 events are listed in Table 7.

7 Non-Standard Contributions at High Q^2

Having presented the essential experimental evidence, we now discuss possible contributions to an excess of events at high Q^2 (high M and y) within and beyond the Standard Model.

7.1 New Contributions in the Standard DIS Model

The standard DIS expectations given in section 4 take into account a systematic error due to a specific choice of the parton density parametrizations. No parton density parametrization compatible with existing experimental DIS data was found to lead to an enhancement of the NC DIS expectation at high masses ($M \gtrsim 180$ GeV) for $Q^2 > 15000$ GeV² beyond the systematic uncertainty quoted in section 4. This is in particular the case for the parametrization CTEQ (4HJ) [34] which was designed to cope with the apparent rise of

	Run # / Event #	M_h	y_h	Q_h^2
1	85987/ 99058	213	.52	23380
2	153720/199055	187	.58	20170
3	163852/20613	157	.75	18650
4	169851/206239	192	.56	20800

Table 7: CC DIS candidates satisfying the kinematic requirement $Q_h^2 > 15000 \text{ GeV}^2$; in the M , y and Q^2 range spanned by these events, the expected resolutions are $\delta M_h/M_h \sim 10\%$, $\delta y_h/y_h \sim 10\%$, $\delta Q_h^2/Q_h^2 \sim 28\%$, not including the systematic uncertainty of 4% associated with the absolute hadronic energy scale.

the di-jet cross-section observed at the Tevatron [45] and leads to an enhancement, compared to MRS (H), of $\lesssim 5\%$ in the above cited M and Q^2 range. In the same context, the parametrization MRS (R2) [33] which assumes a “large” α_s value ($\alpha_s(M_Z^2) \simeq 0.120$) leads to an enhancement of the scaling violation and consequently to a slight reduction of the differential cross-section at high M relative to MRS (H), also within systematic errors.

The MRS (J) parametrization [46] attempts to reproduce the magnitude of the rise of the di-jet cross-section observed in particular in CDF [45] but does not fit existing DIS data (e.g. BCDMS data at high x and low Q^2). It would lead to a cross-section about 20% larger than the values used for this analysis which would still not explain the excess of events observed in the above cited M and Q^2 range.

The statistical significance presented in previous sections for an excess at high Q^2 and/or high M and y is unchanged when using the LEPTO [28] model for the QCD corrections.

The expectations from the standard DIS model have been given under the conservative assumption that the longitudinal structure function F_L is equal to zero. A finite value of F_L either originating from QCD or due to Fermi motion in the proton, would decrease the cross-section at large values of Q^2 and y .

From the above, and given the agreement of the measurement with NC DIS expectation at low M , Q^2 and y (see Fig. 4), there appears to be no mechanism within the standard DIS model framework which would lead to an enhancement of the cross-section at high Q^2 or high y as observed. Within the standard DIS model the only explanation of our result is therefore a statistical fluctuation.

7.2 Physics Beyond the Standard Model

Beyond the Standard Model, the excess at high Q^2 and/or high M and y could be explained by different mechanisms.

New particles could be produced as resonances in the positron-parton system. Prominent examples for new particles with couplings to positron-parton pairs are leptoquarks [47], leptogluons [48] and squarks in R-parity violating versions of Supersymmetry [49]. It should be emphasized that the reconstruction of the invariant mass of such a resonance

is hampered by QED and QCD corrections. An example of such an effect in the form of a narrow s -channel resonance is shown in Fig. 2d as a dotted histogram. The LEGO [50] generator, which was used to produce such a resonance at fixed mass M_{gen} , incorporates initial state QED bremsstrahlung in the collinear approximation and QCD initial and final state parton showers and fragmentation [31]. It moreover properly takes into account the effects of the parton shower masses on the decay kinematics. It can be seen that a resonance would be reconstructed with a systematic shift (typically $\lesssim 5\%$) towards smaller mass values and with a resolution considerably worse than expected from detector effects alone. At the present level of significance, neither the RMS width of the measured events of 8.5 GeV nor the y_e distribution (Fig. 4f), which is expected to extend to larger y_e for a resonance than for NC DIS processes, allow conclusions to be drawn concerning the possibility of resonance formation.

A slight excess is seen in the Q^2 distribution (Fig. 5, Table 2). The virtual exchange of new particles between positrons and partons or possible substructure of fermions inducing contact interactions could all lead to an enhancement of the cross-section at high Q^2 .

8 Summary

Deep-inelastic scattering (DIS) events have been observed in e^+p collisions at very large 4-momentum transfer squared Q^2 , and have been compared with the expectations from the standard Neutral Current (NC) and Charged Current (CC) DIS model.

For $Q^2 \lesssim 15000 \text{ GeV}^2$, the distributions of Q^2 or $M = \sqrt{xs}$ and $y = Q^2/M^2$ are well reproduced by the expectation of standard DIS. At larger momentum transfer ($Q^2 > 15000 \text{ GeV}^2$), 12 NC DIS candidate events are observed where 4.71 ± 0.76 are expected and 4 CC DIS candidate events are observed where 1.77 ± 0.87 are expected. The Poisson probability \mathcal{P} that the signal from standard DIS fluctuates to a number of events equal to or larger than the observed number of events is 6×10^{-3} in the NC case and 0.14 in the CC case.

For the NC candidates, the excess of events is most prominent in a mass window of total width 25 GeV centered at an invariant mass $M \simeq 200 \text{ GeV}$ of the positron-parton system. This mass is consistently determined using different kinematic reconstruction methods, for which only the measured positron, or only the measured angles of the positron and the hadronic system, or only the 4-momenta of the positron and the jet with highest E_T are used. The dominant $e + \text{jet} + X$ topological feature of the events is characteristic of standard neutral current DIS processes. In a mass window of 25 GeV width with a central value of 200 GeV and for $y > 0.4$, 7 events are observed where 0.95 ± 0.18 events are expected. For this and other choices of mass windows and y thresholds, the probability to observe an excess as large as the measured one anywhere in the mass range investigated is of order 1%.

No known detector effect can account for an excess at large Q^2 or can be associated with an excess which occurs preferentially in a restricted range of M .

Given the existing experimental constraints on parton density distributions at high M and lower Q^2 , and given the agreement of the resulting predictions for e^+p DIS which is here reported for Q^2 below 15000 GeV^2 , there is little freedom for an enhancement of the

cross-section at higher Q^2 by different choices for the partonic structure of the proton, by changing the strong coupling constant, or by including higher order corrections.

A new mechanism would be needed to explain an enhancement of the DIS cross-section affecting mostly high Q^2 or high y values. Within the standard DIS model the only explanation of our result is therefore a statistical fluctuation.

Whereas an account of the observation by introducing new physics beyond the standard model of electroweak and strong forces is kinematically possible, the signature of the observed events is identical to DIS and hence a clarification of their nature will have to come from the study of kinematic distributions with larger statistics.

Acknowledgements

We wish to thank the HERA machine group as well as the H1 engineers and technicians who constructed and maintained the detector for their outstanding efforts. We thank the funding agencies for their financial support. We wish to thank the DESY directorate for the support and hospitality extended to the non-DESY members of the collaboration.

References

- [1] ZEUS Collaboration, M. Derrick et al., Z. Phys. C67 (1995) 81; H1 Collaboration, S. Aid et al., Phys. Lett. B353 (1995) 578; ZEUS Collaboration, M. Derrick et al., Z. Phys. C72 (1996) 47.
- [2] H1 Collaboration, S. Aid et al., Z. Phys. C67 (1995) 565.
- [3] H1 Collaboration, S. Aid et al., Phys. Lett. B379 (1996) 319.
- [4] H1 Collaboration, I. Abt et al., Nucl. Phys. B396 (1993) 3; ZEUS Collaboration, M. Derrick et al., Phys. Lett. B306 (1993) 173; H1 Collaboration, T. Ahmed et al., Z. Phys. C64 (1994) 545; H1 Collaboration, S. Aid et al., Phys. Lett. B369 (1996) 173; H1 Collaboration, S. Aid et al., Z. Phys. C71 (1996) 211; ZEUS Collaboration, M. Derrick et al., DESY preprint 96-161 (August 1996) 31pp., to be published in Z. Phys. C.
- [5] H1 Collaboration, I. Abt et al., DESY preprint 93-103 (July 1993) 194pp.; *idem* DESY Internal Report H1-96-01 (March 1996) 157pp.; Nucl. Instr. and Meth. A386 (1996) in print.
- [6] H1 Calorimeter Group, B. Andrieu et al., Nucl. Instr. and Meth. A336 (1993) 460.
- [7] H1 Calorimeter Group, B. Andrieu et al., Nucl. Instr. and Meth. A344 (1994) 492.
- [8] H1 Calorimeter Group, B. Andrieu et al., Nucl. Instr. and Meth. A350 (1994) 57; *idem*, Nucl. Instr. and Meth. A336 (1993) 499.
- [9] H1 SPACAL Group, R.D. Appuhn et al., DESY preprint 96-171 (August 1996) 24pp., to be published in Nucl. Instr. and Meth.

- [10] H1 BEMC Group, J. Ban et al., Nucl. Instr. and Meth. A372 (1996) 399.
- [11] S. Bentvelsen, J. Engelen and P. Kooijman, Proc. of the Workshop Physics at HERA, W. Buchmüller and G. Ingelman (Editors), (October 1991, DESY-Hamburg) Vol. 1 p. 25; K.C. Hoeger, *ibid.* p. 43; and references therein.
- [12] A.D. Martin, R.G. Roberts and W.J. Stirling, Durham Univ. preprint DTP-93-86 and Rutherford Appleton Lab. preprint RAL-93-077 (October 1993) 16pp.; A. D. Martin, R. G. Roberts and W. J. Stirling, Proc. of the Workshop on Quantum Field Theoretical Aspects of High Energy Physics, ed. B. Geyser and E.M. Ilgenfritz (1993), p. 11; from [13] MRS (H): $N_{type}=1$, $N_{group}=3$, $N_{set}=36$, DIS-scheme.
- [13] H. Plochow-Besch, PDFLIB Version 7.07 - W5051, CERN-PPE (December 1996).
- [14] BCDMS Collaboration, A. C. Benvenuti et al., Phys. Lett. B223 (1989) 485; CERN preprint CERN-EP/89-06
- [15] NMC Collaboration, P. Amaudruz et al., Phys. Lett. B295 (1992) 159.
- [16] CCFR Collaboration, A.O. Bazarko et al., Proc. of the XXVIIIth Renc. de Moriond, J. Trân Thanh Vân (Editor), (March 1993) 4pp.
- [17] EMC Collaboration, J. J. Aubert et al., Nucl. Phys. B213 (1982) 31.
- [18] WA70 Collaboration, M. Bonesini et al., Z. Phys. C38 (1988) 371.
- [19] E605 Collaboration, C. N. Brown et al., Phys. Rev. Lett. 63 (1989) 2637.
- [20] CDF Collaboration, F. Abe et al., Phys. Rev. Lett. 68 (1992) 2734; *idem* Phys. Rev. D48 (1993) 2998; Phys. Rev. Lett. 69 (1992) 28; *idem* Phys. Rev. D50 (1994) 5550; Phys. Rev. D50 (1994) 2966; A. Bodek, CDF Collaboration, Proc. of the Int. Workshop on Deep-Inelastic Scattering, Eilat, Israel (1994).
- [21] UA6 Collaboration, G. Sozzi et al., Phys. Lett. B317 (1993) 243.
- [22] H1 Collaboration, I. Abt et al., Nucl. Phys. B407 (1993) 515.
- [23] ZEUS Collaboration, M. Derrick et al., Phys. Lett. B316 (1993) 412.
- [24] Yu. L. Dokshitzer, JETP 46 (1977) 641; V. N. Gribov and L. N. Lipatov, Sov. Journ. Nucl. Phys. 15 (1972) 78; G. Altarelli and G. Parisi, Nucl. Phys. B126 (1977) 298.
- [25] G. Altarelli, R.K. Ellis and G. Martinelli, Nucl. Phys. B143 (1978) 521; *idem* Nucl. Phys. B157 (1979) 461.
- [26] DJANGO 6.2; G.A. Schuler and H. Spiesberger, Proc. of the Workshop Physics at HERA, W. Buchmüller and G. Ingelman (Editors), (October 1991, DESY-Hamburg) Vol. 3 p. 1419.
- [27] HERACLES 4.4; A. Kwiatkowski, H. Spiesberger and H.-J. Möhring, Comput. Phys. Commun. 69 (1992) 155.

- [28] LEPTO 6.5; G. Ingelman, Proc. of the Workshop Physics at HERA, W. Buchmüller and G. Ingelman (Editors), (October 1991, DESY-Hamburg) Vol. 3 p. 1366.
- [29] ARIADNE 4.08; L. Lönnblad, Comput. Phys. Commun. 71 (1992) 15.
- [30] G. Gustafson and U. Pettersson, Nucl. Phys. B306 (1988) 746; *idem*, *addendum* Lund University preprint LU-TP-87-19, (October 1987) 4pp.; B. Andersson et al., Z. Phys. C43 (1989) 625.
- [31] JETSET 7.3 and 7.4; T. Sjöstrand, Lund Univ. preprint LU-TP-95-20 (August 1995) 321pp; *idem*, CERN preprint TH-7112-93 (February 1994) 305pp.
- [32] HECTOR 1.00; A. Arbuzov et al., Comput. Phys. Comm. 94 (1996) 128
- [33] A.D. Martin, W.J. Stirling and R.G. Roberts, Phys. Lett B387 (1996) 419; from [13] MRS (R1): $N_{type}=1, N_{group}=3, N_{set}=53$, \overline{MS} scheme; MRS (R2): $N_{type}=1, N_{group}=3, N_{set}=54$, \overline{MS} scheme.
- [34] H. L. Lai et al., Phys. Rev. D55 (1997) 1280; from [13] CTEQ4M: $N_{type}=1, N_{group}=4, N_{set}=34$, \overline{MS} scheme; CTEQ4HJ: $N_{type}=1, N_{group}=4, N_{set}=40$, \overline{MS} scheme.
- [35] M. Glück, E. Reya and A. Vogt, Z. Phys. C67 (1995) 433; from [13] GRV94HO: $N_{type}=1, N_{group}=5, N_{set}=6$, \overline{MS} scheme.
- [36] W.A. Bardeen et al., Phys. Rev. D18 (1978) 3998.
- [37] H. L. Lai et al., Phys. Rev. D55 (1997) 1280 from [13] $N_{type}=1, N_{group}=4, \overline{MS}$ scheme; $N_{set}=35$, CTEQ (4A1); $N_{set}=36$, CTEQ (4A2); $N_{set}=37$, CTEQ (4A3); $N_{set}=38$, CTEQ4 (A4); $N_{set}=39$, CTEQ (4A5).
- [38] HELIOS 1.0; J. Blümlein, Proc. of the Workshop Physics at HERA, W. Buchmüller and G. Ingelman (Editors), (October 1991, DESY-Hamburg) Vol. 3 p. 1272; Z. Phys. C65 (1995) 293.
- [39] TERAD 91; A. Akhundov et al., Proc. of the Workshop Physics at HERA, W. Buchmüller and G. Ingelman (Editors), (October 1991, DESY-Hamburg) Vol. 3 p. 1285, DESY preprint 94-115 (July 1994).
- [40] H1 generator based on EPVEC 1.0; U. Baur, J.A.M. Vermaseren and D. Zeppenfeld, Nucl. Phys. B375 (1992) 3.
- [41] T. Sjöstrand, CERN-TH-6488 (1992), Comp. Phys. Comm. 82 (1994) 74.
- [42] M. Glück, E. Reya and A. Vogt, Phys. Rev. D45 (1992) 3986; *idem*, Phys. Rev. D46 (1992) 1973.
- [43] S. Baranov et al., Proc. of the Workshop Physics at HERA, W. Buchmüller and G. Ingelman (Editors), (October 1991, DESY-Hamburg) Vol. 3, p. 1478; J.A.M. Vermaseren, Nucl. Phys. B229 (1983) 347.

- [44] C. F. v. Weizsäcker, *Z. Phys.* 88 (1934) 612; E. J. Williams, *Phys. Rev.* 45 (1934) 729; P. Kessler, *Nuovo Cim.*, 17 (1960) 809; C. Carimalo et al., *Phys. Rev. D*10 (1974) 1561; *Phys. Rev. D*18 (1978) 2443; P. Bussey, *Proc. of the Workshop Physics at HERA*, W. Buchmüller and G. Ingelman (Editors), (October 1991, DESY-Hamburg) Vol. 1, p. 629.
- [45] CDF Collaboration, F. Abe et al., *Phys. Rev. Lett.* 77 (1996) 438; G.C. Blazey, D0 Collaboration, *Proc. of the XXXIst Renc. de Moriond*, J. Trân Thanh Vân (Editor), (March 1996) 11pp.
- [46] E.W.N. Glover et al., *Phys. Lett.* B381 (1996) 353.
- [47] W. Buchmüller, R. Rückl and D. Wyler, *Phys. Lett.* B191 (1987) 442.
- [48] H. Fritzsche and G. Mandelbaum, *Phys. Lett.* B102 (1981) 319; U. Baur and K.H. Streng, *Z. Phys.* C30 (1986) 325.
- [49] J. Butterworth and H. Dreiner, *Nucl. Phys.* B397 (1993) 3, and references therein.
- [50] LEGO 0.02; K. Rosenbauer, thesis RWTH Aachen, PITHA preprint 95/16 (July 1995).